JOURNAL OF THERMOPHYSICS AND HEAT TRANSFER
Vol. 16, No. 3, July–September 2002

Operational Behavior of Inductively Heated Plasma Source IPG3 for Entry Simulations

G. Herdrich,* M. Auweter-Kurtz,† H. L. Kurtz,‡ T. Laux,§ and M. Winter§
University of Stuttgart, D-70550 Stuttgart, Germany

The design of the plasma wind tunnel (PWK3), its inductively heated plasma generator (IPG3), and experimental results using O_2 and CO_2 as operational gases are described. Various operational conditions (mass flow rate, frequency) were applied. The thermal plasma powers measured with a calorimeter in the chamber of PWK3 are presented, leading to the possibility to determine efficiencies. When the power was varied, two discrete operational transitions were observed. The simultaneous differences in the discharge behavior of IPG3 are represented by sudden changes of parameters such as calorimetric powers and local heat fluxes measured with a stationary heat flux probe in the chamber of the facility. Additionally, the cooling power of the IPG3 plasma tube is presented. Here, a plasma stabilization effect appearing with the second operational transition was observed when the tube cooling power decreased suddenly despite the simultaneous increase of the plasma power in the chamber. An imaging spectrometer measuring the radial intensity of the plasma through an axial optical window of IPG3 was used. Both the operational behavior, in particular the stabilization effect, and the heat flux measurements show that PWK3 enables high-enthalpy tests for both basic thermal protection material tests and atmospheric entry simulation of spacecrafts.

Nomenclature

A	=	area, m^2
a	=	thickness of coupling zone, m
C	=	capacity, F
c	=	heat capacity, J/(kg K)
d	=	diameter, m
E	=	electric field, V/m
F	=	force, N
f	=	frequency, Hz
H	=	magnetic flux, A/m
I	=	current, A
j	=	current density, A/m^2
m	=	mass, kg
n	=	number of coil windings
P	=	power, W
R	=	resistance, W
r	=	radial position, radius, m
T	=	temperature, K
t	=	time, s
U	=	voltage, V
V	=	volume, m^3
δ	=	skin depth, m
η	=	efficiency
λ	=	eigenvalue
μ_0	=	permeability, Vs/Am
ρ	=	density, kg/m^3
σ	=	electrical conductivity, S/m
ω	=	angular frequency, 1/s

Subscripts and Superscript

A	=	resonant circuit anode
cal	=	calorimeter
in	=	inlet
ind	=	induced
inn	=	inner tube wall
out	=	outlet
L	=	Lorentz force
p	=	pressure
tot	=	total
wall	=	inner wall of tube
$\cdot$	=	derivatives with respect to time

Introduction

ON entering the atmosphere of celestial bodies, spacecraft encounter gases at velocities of several kilometers per second, thereby being subjected to great heat loads. This makes it necessary to use high-temperature thermal protection systems (TPS) to prevent the destruction of the space vehicle. The TPS as well as the environment (plasma) during the entry have to be investigated by computational and ground-facility-based simulations. The five Institut für Raumfahrtsysteme (IRS) plasma wind tunnels (PWK) 1–5 are such ground facilities. They are stationary test facilities in which high-enthalpy flows are produced to reproduce the thermal, aerodynamic, and chemical load on the surface of a space vehicle entering a celestial body's atmosphere. Different types of plasma generators such as magnetoplasmadynamic plasma generators (MPG), thermal arcjet devices (TPG), and inductively heated plasma generators (IPG) have been developed at IRS. MPGs allow gas flows to be produced at high enthalpies. They are mainly used to investigate the erosion of radiation-cooled heat shield materials, as well as the behavior of ablative materials. A TPG producing moderate enthalpies and higher stagnation pressures to simulate the follow-on flight path is in operation.[1]

The application of an IPG has two major advantages. First, researchers are aware that the catalytic behavior of TPS materials is one of the main topics to be investigated in the future. A main part of the heat flux seen by a TPS material derives from the recombination of atomic plasma species. When the IPG is used, the related heat flux measurements are not falsified by impurities as with electrode plasma generators. Catalytic mechanisms of single gases of an atmosphere can be investigated. Applications in the range of

Presented as Paper 99-3497 at the AIAA 33rd Thermophysics Conference, Norfolk, VA, 28 June–1 July 1999; received 12 April 2001; revision received 16 November 2001; accepted for publication 8 December 2001.

*Research Engineer, Institut für Raumfahrtsysteme, Pfaffenwaldring 31; herdrich@irs.uni-stuttgart.de. Member AIAA.
†Professor, Institut für Raumfahrtsysteme, Pfaffenwaldring 31. Senior Member AIAA.
‡Head of Laboratory, Institut für Raumfahrtsysteme, Pfaffenwaldring 31.
§Research Engineer, Institut für Raumfahrtsysteme, Pfaffenwaldring 31.

plasma diagnostics on the ground and in situ (flight experiments), such as heat flux measurements using materials with different, but well-known catalycities, can be performed. Here, it is possible to determine atomic species concentrations within the plasma.[2,3]

The second advantage is to be seen in the possibility of performing entry simulations for celestial bodies such as Mars or Venus, where there are rather reactive gas components such as CO_2. IRS has already performed high-enthalpy CO_2 tests, which showed that the PWK3–IPG3 is able to perform entry simulations for atmospheres containing CO_2. This enables participation in campaigns such as Venus Sample Return Missions, Mars Mini-Probes,[4,5] or Mars Sample Return Mission and Mars Ballon Mission, which are presently under investigation.[6,7]

Measurement techniques, such as intrusive probes and nonintrusive methods, such as emission spectroscopy, laser-induced fluorescence, and Fabry–Perot interferometry, are used to investigate the plasma flows. Besides the nonintrusive measurement techniques, mass spectrometry and electrostatic and radiation probes also belong to the group of intrusive measurement techniques. The mechanical probes are among the most important instruments for plasma-diagnostic measurements and are, therefore, often used. In addition to the standard sample support system that carries the TPS material sample to be tested, pitot pressure probes, aerodynamic wedge probes (Mach number determination), heat flux probes, enthalpy probes, and solid-state electrolyte probes for determining the oxygen particle pressure are used to characterize the plasma. All of these probes can be installed at IRS on movable platforms inside the PWKs. Electrostatic probes are used to ascertain plasma potential, electron density and temperature, and energy distribution of electrons, ion temperature, and flow velocity and direction. The measurement principle is based on an active influence of the plasma boundary layer that forms on the probe. The use of radiometric probes is unavoidable when the radiation heat flux can not be neglected compared to the convective share of the heat flux. This occurs when, during sample return missions, the entry speed into the Earth's atmosphere is especially high or when the atmosphere of another celestial body (which is to be entered) contains strong radiating species, for example, the atmosphere of Titan.[8] The measurement of the plasma power of an inductively heated plasma is rather difficult because the power factor of the circuit is unknown. However, rough estimations can be obtained using the plasma-off mode method. To measure the plasma power, the resonant circuit can be run in the no-plasma mode. In a second step, the resonant circuit can be run in the plasma mode with the tube conditions kept constant. The difference of both power values leads to an estimation of the plasma power.[9,10] However, possible shifts in the working point of the triode may occur. Therefore, IRS developed a calorimeter that has been used within the oxygen measurement campaign presented in this paper.

Setup of PWK3 and IPG3

The basic setup of PWK3 is shown in Fig. 1. The whole facility consists of the plasma source and the vacuum chamber. The size of the vacuum chamber is 2 m in length and 1.6 m in diameter. Optical access to the vacuum chamber is provided to measure and observe the plasma. The plain lid of PWK3 (left side of chamber, Fig. 1) carries the IPG and the external resonant circuit, consisting of the capacitors with the connection to the plasma generator.

The right-side flange of the vacuum chamber is connected to the four-stage vacuum pump system. It is used to simulate pressures at altitudes up to 90 km. The suction power of the pumps is 6.000 m^3/h at atmospheric pressure and reaches 250.000 m^3/h at 10 Pa measured at the intake pipe of the system, which has a diameter of 1 m. The base pressure of the system is 0.5 Pa. The desired tank pressure can be adjusted between the best achievable vacuum and 100 kPa by removing pumps from the circuit and/or mixing additional air into the system close to the pumps.

The external resonant circuit is cooled by a water cooling circuit. With this, the capacitors, which have a capacity of 6 nF $\pm$ 20% each, and the induction coil are cooled. The resonant circuit is built in Meissner-type switching (see Ref. 11) using a metal–ceramic triode

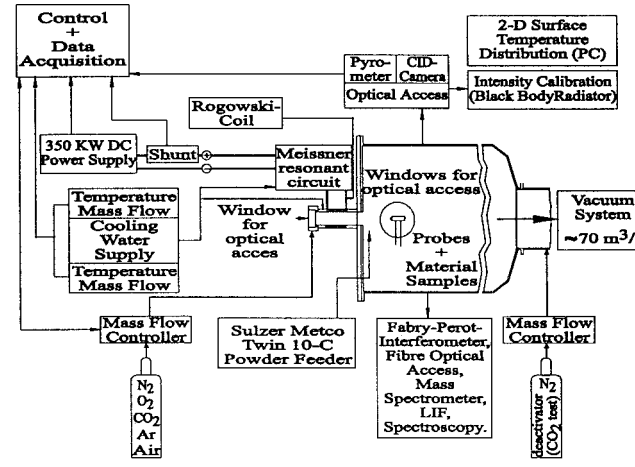

Fig. 1 Scheme of plasma wind tunnel PWK3.

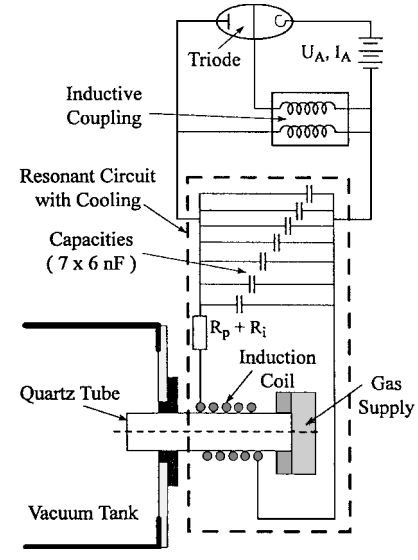

Fig. 2 Scheme of the PWK3 Meissner-type resonant circuit.

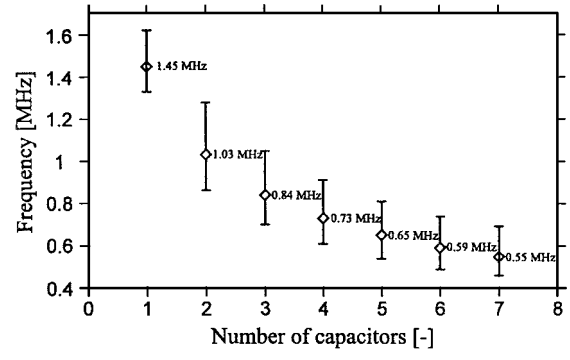

Fig. 3 Nominal operating frequencies for different capacitor switchings, $L_{inductor} \approx 2\ \mu H$.

with an oscillator efficiency of about 75% (Fig. 2).[12] Its nominal frequency can be changed by switching the number of capacitors (Fig. 2), as well as by the use of coils with different inductivities. The error bars in Fig. 3, which show the seven different nominal frequencies, take into account the tolerances of the capacitors.[12] The whole circuit is switched to a 375-kW power supply. The incoming dc anode power or plate power is the tube's plate input and can be adjusted by control of the dc anode voltage.

For the present investigations, the frequency has been tuned to the nominal frequencies of 0.73 MHz (four capacitors) and 1.45 MHz

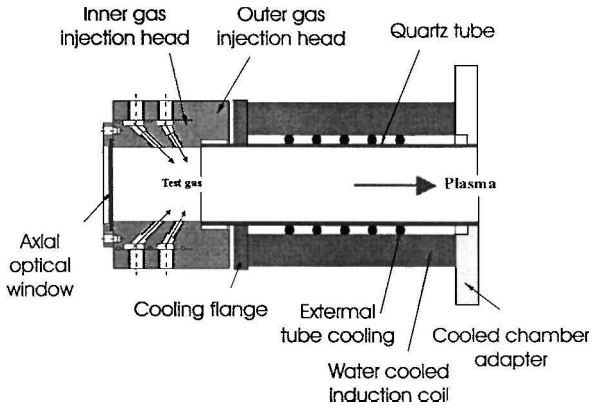

Fig. 4 View of the plasma source IPG3.

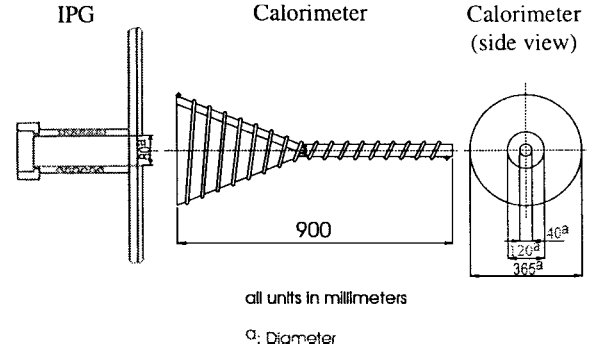

Fig. 5 Scheme of the calorimeter in PWK3.

(one capacitor) using a water-cooled five-turn coil with a length of about 120 mm. This coil geometry leads to an inductivity of about 2 μH. IPGs basically consist of an induction coil surrounding a plasma container and capacitors, as schematically shown in Fig. 2.

The resonant circuit is fed by an energy supply. With IPG3, an rf source is provided where the coil is closer to the plasma than it was with previous designs, which reduced the electromagnetic field loss. The water cooling system surrounds both the induction coil and the plasma container. The alternating current in the coil induces a mostly azimuthal electric field inside the tube. This electric field initiates an electric discharge in the gas, which is injected at one side into the tube (Fig. 4). The produced plasma is expanded into the vacuum chamber. The electric discharge in the plasma is carried by mostly azimuthal eddy currents. Both the current amplitude and, thus, the Ohmic heating depend on the electric conductivity of the plasma and the resonant frequency of the electric circuit. Various gas injection angles are achievable by replacing the inner gas injection head with others that have different bore angles (Fig. 4). Therefore, the influence of the injection angle on the operational behavior of IPG3 can be studied. It is evident that the plasma is continuously swept away by an axially injected gas.[13] Hence, the plasma can be stabilized using a tangential injection of the gas. This produces a swirl gas flow leading to a pressure and density decrease toward the generator's axis. Lower pressure can be expected in the tube's center. Thus, on the one hand, the plasma partially recirculates, and on the other hand, it is partially kept away from the inner surface of the tube. Hence, a lower heat load of the tube can be achieved, and higher power can be applied. An axial optical access through the inner injection head enables investigations of the plasma inside the generator. The spectroscopic measurements to be given have been performed using this optical window, schematically shown in Fig. 4. The tube cooling system is transparent; therefore, the position of the plasma flame within the tube can be observed with regard to different operating parameters such as chamber pressure, gas, mass flow, and anode power. Additionally, this feature is supported by the axial optical window. The total length of IPG3 is about 0.35 m; its diameter is about 0.1 m.

The quartz tube contains the produced plasma that leaves the generator through the water-cooled chamber adapter. The induction coil is connected to the external resonant circuit (Figs. 1 and 2), which delivers power and cooling water for IPG3. Furthermore, both the tube and the coil are surrounded by the external tube cooling, which protects the quartz tube from overheating. The water and an additional cage around the generator serve as an rf-radiation protection shield.

Measurement Techniques

The variety of probes and optical diagnostic techniques that have been developed and qualified at IRS has been surveyed in the Introduction. More precise descriptions have been made in Ref. 8. In the section to follow, the measurement techniques that have been used for the measurements are described.

The Meissner-type resonant circuit is supplied by the dc P_A, which is measured during the operation of the device.[11] The anode voltage U_A is a controlled constant. Hence, the anode current I_A results from the load of the resonant circuit (plasma) and the accompanying operating conditions (Fig. 2).

Thermal powers such as tube cooling power, resonant circuit power, and plasma power are measured using resistance thermometers (Fig. 1). They are electrically sealed and installed at an acceptable distance from the plasma source to prevent disturbing signals from the rf field. Additionally, the cooling water flow rates are measured.

The mass flow of the test gas (Fig. 1) and the pressure of the inner gas injection head are measured as well. A Rogowski coil can be used to determine the operational frequencies (see Ref. 10). A cavity calorimeter has been developed to determine the (induced) thermal plasma power in the PWK3 vacuum chamber (Fig. 5). The working principle is quite simple. The plasma enters the copper cavity, which is shaped like a cone, through a hole. The diameter of the hole is 120 mm, which is roughly 25% bigger than the plasma beam. The distance between the calorimeter and the plasma outlet of IPG3 is about 100 mm. This is necessary because lower distances can result in retroactions that manipulate the discharge behavior of the plasma generator (discharge behavior, also see Ref. 10). Copper is used due to the very high specific heat conductivity and due to its high catalycity.[14] The copper walls are heated through radiation, convection, and recombination. The whole cavity is equipped with spiral copper tubes that guide the cooling water, which cools the copper wall.

With the measured cooling exit temperature, the cooling inlet temperature, and the cooling water flow rate, the plasma power can be calculated:

$$P_{\text{cal}} = c_{p,\text{water}}\, \dot{m}_{\text{water}} (T_{\text{out}} - T_{\text{in}}) \tag{1}$$

Here $\dot{m}_{\text{water}}$ is the cooling water mass flow rate, $c_{p,\text{water}}$ is the heat capacity, T_{out} is the cooling water outlet temperature, and T_{in} is the cooling water inlet temperature.

It is evident that this kind of calorimetric plasma power measurement is accompanied by inaccuracies such as radiation loss or imperfect heat exchange between the plasma and the copper wall. However, the estimation of the radiation loss showed an inaccuracy below 1% due to the low cooling water temperatures. The overal accuracy of both the calorimeter and the heat flux measurement is on the order of 10% when the accuracies of the applied measurement techniques are taken into account, such as the resistance thermometers and the water flow meter. This accuracy can be estimated using a differential for ΔP_{cal} with the differences $\Delta \dot{m}_{\text{water}}$ and $\Delta(T_{\text{out}} - T_{\text{in}})$. The heat flux measurement is even less accurate due to the adjustment of the probe and the sensor area accuracy ΔA [see Eq. (2)].

The heat flux probe (Fig. 6) used for this investigation is geometrically similar to the material support system used for material tests. The probe area of the calorimetric probe is given by the front side of small inserts into the front plate of a water-cooled support, which provides thermal shielding and insulation for other surfaces of the

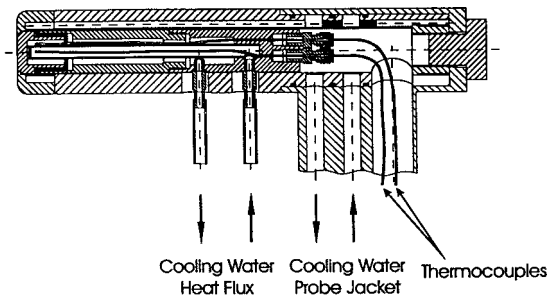

Fig. 6 Stationary heat flux probe.

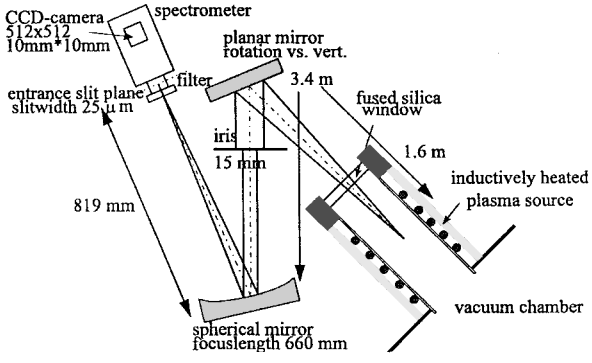

Fig. 7 Spectroscopic setup for the IPG3 measurement.

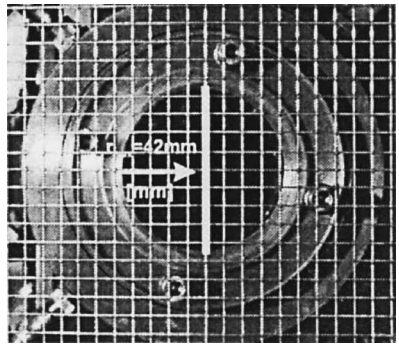

Fig. 8 Spectroscopically observed region of the IPG3 optical access (shown by arrow).

inserts. When the probe is moved into the plasma jet, only the heat flux to the insert probe area of the front side facing the plasma is measured. The area of the insert has a 22.1-mm diameter. Thus,

$$\dot{q} = c_{\text{water}} \dot{m}_{\text{water}} (T_{\text{out}} - T_{\text{in}})/A \tag{2}$$

A spectrometer for determining radial intensity distribution of selected species has been used. The measurements were performed through the optical window of IPG3 (Figs. 1 and 3). The total spectroscopic setup has already been used similarly in previous PWK measurement campaigns.[15] Figure 7 shows the spectroscopic experimental setup and the related geometries as applied for the IPG3 radial intensity profile.

To determine effects of scattered light within the intensity calibration, spectral filters can be placed in the optical path. The calibration values of the tungsten band lamp used for the intensity calibration are normalized by the measured area on the lamp, the measured solid angle, and the wavelength covered by a detector pixel. The measured wavelengths on each pixel have been taken from the wavelength calibration. The calibration lamp was placed at the same distance and in a similar geometric position as the position of IPG3. The optical setup is adjusted using a HeNe-laser beam entering the spectrometer at the second exit slit. Therefore, the laser beam has to take the reverse optical path. This, however, enables the measurement position inside the IPG3 to be checked.

A grating with 50 grids/mm, blazed to 300 nm, was used, which yielded a spectral resolution of about 1.2 nm. Correspondingly, a wavelength measurement interval from 200 up to 800 nm was achieved. Measuring the left half of the tube was achieved by adjusting the mirrors (Fig. 8). This is sufficient under the evident assumption of symmetrical radial intensities over the inner radius of the plasma generator's tube. The spatial resolution of the measurement was roughly 1 mm. A Thompson 512×512 pixel charge-coupled device array with a 10×10 mm measurement area was used.

Behavior of an IPG Derived from One-Dimensional Calculation

It is evident that the magnetic field of the induction coil and the plasma current influence each other. The induced field of the plasma current counteracts against the magnetic field of the coil. Therefore, plasma current decreases from the inner tube wall to the middle of the tube (along the radius). This effect is called the skin effect. It is possible to formulate analytical statements under several assumptions, such as the constant electrical conductivity of the plasma over the cross area of the plasma tube. According to the law of induction, it can be deduced that the current density goes down to zero if the radial distance r to the tube's middle is zero. Here, the skin effect leads to an almost exponential decrease of the current density.

Figure 9 shows the situation for a resonant circuit coil with five turns. The produced magnetic flux changes its direction with the change of the current polarity in the induction coil. However, the plasma current direction changes its direction as well. In the estimative calculations to follow, a Lorentz force F_L is derived. This force seems to play a role for the IPG3 operational behavior with O_2. Note that for both cases in Fig. 9 the Lorentz forces points in the direction of the radius toward the center of the tube. Because both the magnetic flux H and the plasma current I_{plasma} change their direction simultaneously, the resulting Lorentz force does not change its direction. We assume a constant electrical conductivity σ and the permeability μ_0. The cylinder length (integration volume) shall be identical to the coil length l. The magnetic flux vector is parallel to the tube, that is, directed in the axial direction of the IPG. A sinusoidal magnetic flux H shall be assumed:

$$H(t) = H_{\max} \cos(\omega t) \tag{3}$$

The Maxwell equations are

$$-\frac{\partial H}{\partial r}(t) = j(t) \tag{4}$$

$$\frac{\partial E}{\partial r}(t) = -\mu_0 \frac{\partial H}{\partial t}(t) \tag{5}$$

if a large discharge diameter is assumed. In its simplified version, Ohm's law is

$$E(t) = j(t)/\sigma \tag{6}$$

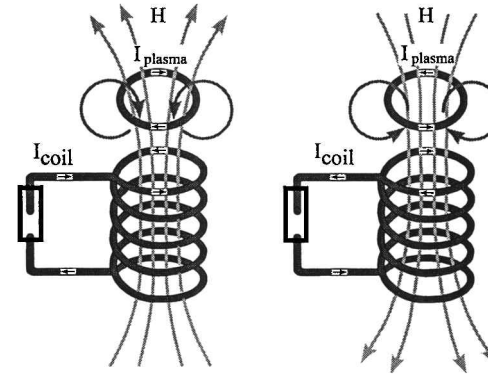

Fig. 9 Electromagnetic behavior of an IPG.

With the simplification/assumption that the current density is sinusoidal, we can write

$$j(t,r) = j_{\max} e^{i\omega t} e^{-\lambda r} = j_{\max}(r) e^{i\omega t} \tag{7}$$

The combination of Ohm's law and the Maxwell equations leads to the following differential equation:

$$\frac{\partial^2 j}{\partial r^2}(t) = \mu_0 \sigma \frac{\partial j}{\partial t}(t) \tag{8}$$

With Eq. (7), this leads to

$$\frac{\partial^2 j}{\partial r^2}(t) = i\omega\mu_0\sigma j(t) \tag{9}$$

This leads to

$$\lambda = \sqrt{i}\sqrt{\omega\mu_0\sigma} = (i+1)\sqrt{\pi f \mu_0 \sigma} = (1+i)/\delta \tag{10}$$

whereas the skin depth can be formulated by

$$\delta = 1\Big/\sqrt{\pi\mu_0\sigma f} \tag{11}$$

Therefore, for the current density we get

$$j = j_{\max}(t)\exp[-(r/\delta)]\exp[-i(r/\delta)] \tag{12}$$

However, the complex term of Eq. (12) describes the phase relationship only. This, for our further considerations,is of little importance:

$$|j| = j_{\max}(t)\exp[-(r/\delta)] \tag{13}$$

The total plasma current can then be calculated,

$$I_{\text{plasma}} = \left(1\Big/\sqrt{2}\right) j_{\max} l \delta \tag{14}$$

The volumetric power is

$$\frac{\partial P_{\text{ind}}}{\partial V} = \frac{1}{\sigma}|j|^2 \tag{15}$$

Integration yields

$$P_{\text{ind}} = (\pi d/l\delta\sigma) I^2_{\text{plasma}}(t)(1 - (\delta/d)\{1 - \exp[-(d/\delta)]\})$$

$$= R_{\text{plasma},zyl} I^2_{\text{plasma}} \tag{16}$$

The term

$$P_{\text{ind,part}}/P_{\text{ind,total}} = 1 - (\delta/2a)\{1 - \exp[-(2a/\delta)]\}$$

describes the share of induced plasma power within a ring of the thickness $a < R$ at the inner tube wall for the condition $\delta \ll R$. Figure 10 shows the entire history of this function.

Here, one of the most severe problems of the IPG becomes obvious. Within the first two skin depths ($a = 2\delta$), more than 75% of the total plasma power is induced. This explains the problem of the plasma containment of an IPG (tube cooling by cooling systems or special gas injection or both).

In addition, a calculation can be performed based on the coil current I_{coil}. This is more challenging and leads to an estimated one-dimensional equation that depends on Bessel functions (see Ref. 16). Corresponding sources state the following equation (Fig. 11):

$$I_{\text{plasma}} \approx m(d/\delta) n I_{\text{coil}} \tag{17}$$

In the following section, the Lorentz force shall be considered. The Lorentz density is

$$\boldsymbol{F}_L = \boldsymbol{j}_{\text{plasma}} \times \boldsymbol{B} = \mu_0 \boldsymbol{J}_{\text{plasma}} \times \boldsymbol{H}_{\text{coil}} \tag{18}$$

Because the vectors are perpendicular, Eq. (18) can be written as

$$F_L = \mu_0 \int j_{\text{plasma}} H_{\text{coil}} A \, \mathrm{d}s \tag{19}$$

When Eq. (16) is used, this leads to

$$F_L \approx \sqrt{2}\mu_0\left(\delta^2\sigma\Big/r_{\text{inn}}\right) P_{\text{ind}} f(d/\delta) \tag{20}$$

and a function f can be formulated:

$$f\left(\frac{d}{\delta}\right) \approx \frac{1}{\sqrt{m(d/\delta)}} \frac{(d/2\delta) + \exp[-(d/2\delta)] - 1}{1 - (\delta/d)\{1 - \exp[-(d/\delta)]\}}$$

$$\approx [(d/2\delta) - 1], \qquad \text{if} \qquad d/\delta \geq 3 \tag{21}$$

In Fig. 12, Eq. (22) is calculated for different σ. It is evident that the a value of 10^3 1/(Ωm) is rather low if a typical high-enthalpy plasma is assumed. This together with the resulting $d/\delta > 3$ allows a simplification of Eq. (20) leading to the estimative Eq. (22) for the Lorentz forces of an IPG:

$$F_L/P_{\text{ind}} \approx \sqrt{2}\Big/\pi f[(1/\delta) - (1/r_{\text{inn}})] \tag{22}$$

The function of an IPG is explained in this section using a simple one-dimensional model of estimative nature. In fact, the experiments showed that there is a discharge behavior such that there are three

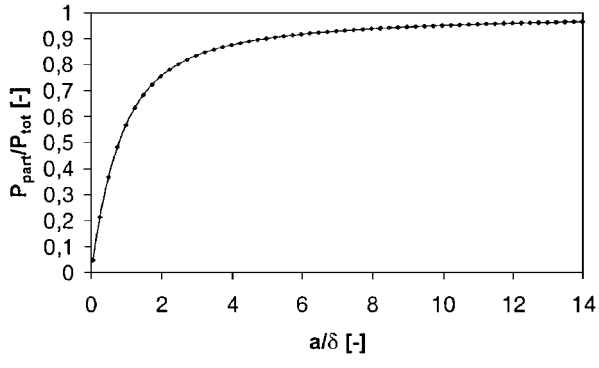

Fig. 10 Spatial deposition profile of induced plasma power within a ring of the thickness a from the inner plasma tube wall.

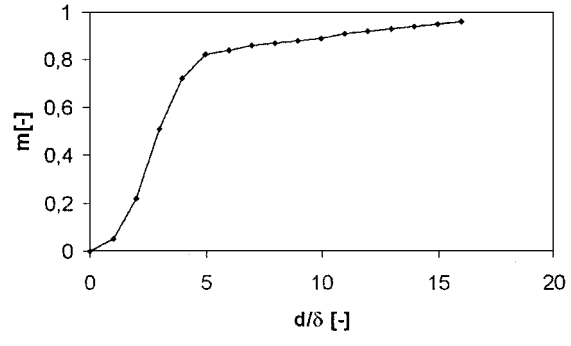

Fig. 11 Function $m(d/\delta)$.

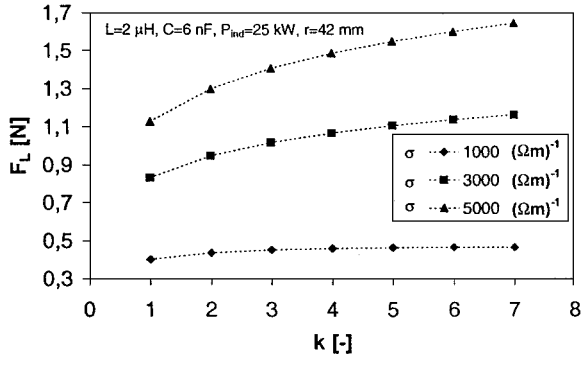

Fig. 12 F_L depending on the number of capacitors (here PWK3–IPG3 configuration) for different σ.

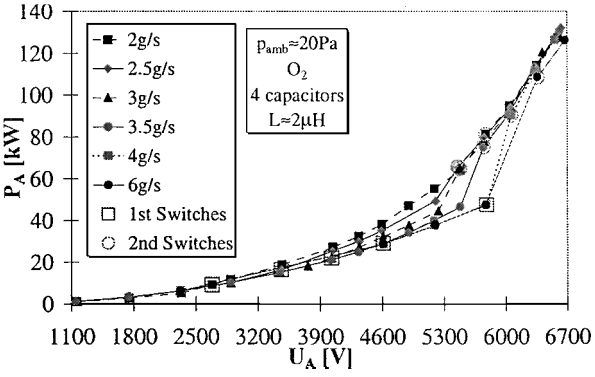

Fig. 13 P_A **vs** U_A **for** O_2 **plasmas using four capacitors (**f **= 0.73 MHz) for different mass flow rates.**

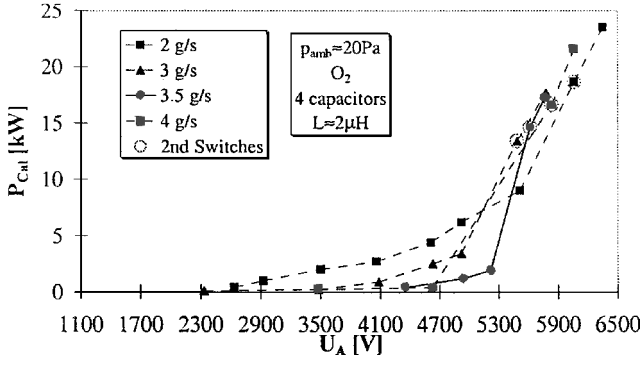

Fig. 14 Calorimetric plasma power (in the vacuum chamber) vs U_A **for** O_2 **plasmas using four capacitors (**f **= 0.73 MHz) for different gas mass flows.**

operational modes (see "Results" section). Note that with the transition from the second to the third mode (second switch) the thermal power increases by a factor of 2–7 while the U_A change was about 500 V (see Figs. 13 and 14). The power increase has its origin in an adaption of the resonant circuit, which means that there is a decisive increase in the electrical conductivity of the plasma load. Although P_{ind} increases suddenly and by several factors, the P_{tube} decreases. This leads to the statement that there might be a stabilization effect that maybe driven by the increased Lorentz forces. Most likely this effect also depends on the flow (not included in the present model).

Equation (22) shows that, with the increase of the thermal plasma power, the Lorentz forces increase as well by several factors, according to the model. The equation depends on frequency and induced plasma power P_{ind}. However, note that P_{ind} itself is a function of f. In Fig. 12, we used a typical value for the total thermal plasma powers as measured in this campaign and presented in the section to follow. The inductive heating industry uses about the same dependencies (such as proportionality of F_L and P_{ind}). Real F_L effects have been observed in the range of inductive melting of metals. Here, a movement of the liquid melt is initiated by the Lorentz forces (see Ref. 17).

Results

Two major test campaigns have been performed. The first was performed with pure oxygen plasma and the second with CO_2 plasma. Most experiments were done at minimum ambient pressure. These experiments were performed using four capacitors ($f = 0.73$ MHz). To a certain extent, both gases were also investigated using one capacitor ($f = 1.45$ MHz) to get a comparison of both nominal frequencies.

Generally, the IPG3 shows a discharge behavior. The transition between low-power mode and high-power mode discharge and the radial intensity distribution for air has already been presented.[10] Note that this transition also appears for O_2 and CO_2. The point of the first transition (first switch) depends on pressure, frequency, and mass flow rate of the test gas.

Experimental Results with O_2

During the experiments with O_2, three major observations were made:

1) The higher the mass flow rate was, the lower the anode powers were at the same anode voltages.

2) The first discharge switch[10] depends on the mass flow rate and moves toward higher anode voltages with increasing mass flow. This first switch can be noticed as the intensity of the plasma increases suddenly.

3) A second switch was observed. This second switch has only a weak dependency on the mass flow rate of the gas. However, the second switch is accompanied by a massive anode power jump. The corresponding ΔP_A increases with the mass flow. It is observable by sight as well. The plasma changes its color slightly and becomes brighter.

In Figs. 13–18, curves for different mass flow rates are shown. The transitions (called switches) are marked by enlarged open symbols that surround the corresponding data point of the curve. Each of these symbols stands for one switch belonging to one mass flow rate condition. The first switches are badly resolved for Figs. 13, 14, 17, and 18. Indeed, for the intended operation as an entry simulation facility, the second and the third regime after the first switch or even second switch are more important due to the high plasma enthalpies. For more details concerning the first switch, see Ref. 10.

Figure 13 shows the measured anode powers for different oxygen mass flow rates.

Both the first (Figs. 15 and 16) and the second switch (Figs. 13–18) are accompanied by rather sudden changes of corresponding parameters such as heat flux, tube pressure, and tube cooling. However, the biggest changes appear with the second switch (Fig. 15). Figure 15 shows one of the most interesting results. The overall tube cooling decreases with increasing mass flow rates. Furthermore, a sudden decrease of the tube cooling appears with the second switch. This decrease seems to become larger with increasing mass flows. Whereas anode power (Fig. 13) and, in particular, the thermal power

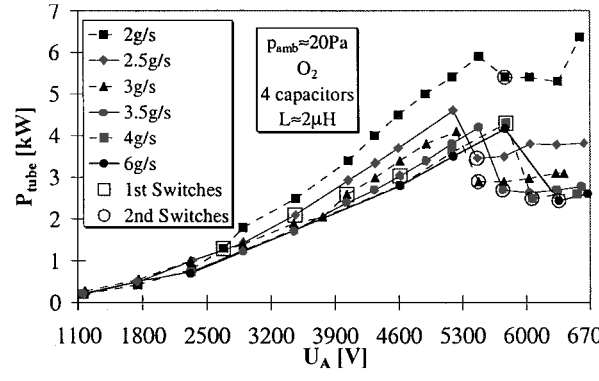

Fig. 15 P_{tube} **vs** U_A **for** O_2 **plasmas using four capacitors (**f **= 0.73 MHz) for different gas mass flows.**

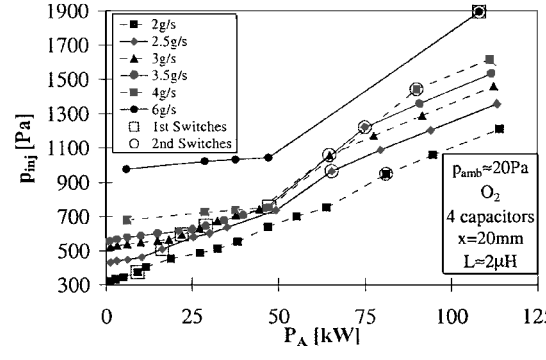

Fig. 16 Tube pressure vs U_A **for** O_2 **plasmas using four capacitors (**f **= 0.73 MHz) for different gas mass flows.**

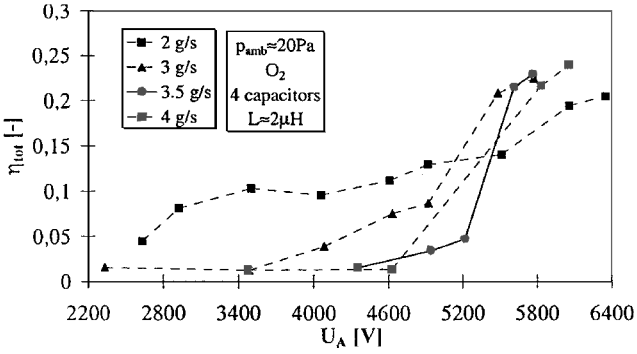

Fig. 17 Total efficiency vs U_A for O_2 plasmas using four capacitors ($f = 0.73$ MHz) for different gas mass flows.

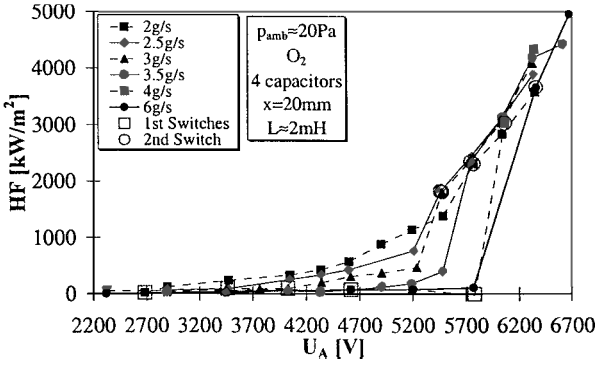

Fig. 18 Heat flux vs U_A for O_2 plasmas using four capacitors (f = 0.73 MHz) for different gas mass flows.

(Fig. 14) indicate that the plasma power increases suddenly with the second switch, it seems contradictory that P_{tube} decreases.

The definition of a total efficiency

$$\eta_{tot} = P_{cal}/P_A \tag{23}$$

seems useful (Fig. 17).

It is evident that a sudden increase of the plasma power appears despite the simultaneous decrease of P_{tube}. This result becomes very interesting if Eq. (22) is considered. In fact, the total induced plasma power [the sum of P_{tube} and P_{cal} (in the chamber)] increases suddenly with the second switch. Corresponding to Eq. (22), a sudden increase of the Lorentz forces occurs. This effect probably leads to a pinch effect that keeps the plasma away from the inner tube wall. Similar effects have also been observed in the range of inductive metallic melting.[17]

Figure 18 shows the measured heat fluxes at about 25 mm away from the IPG3 plasma outlet. Here, the sudden increase of heat flux confirms the earlier statements, too. In Fig. 16, the inner tube pressure is shown. Here, both the increase with the first as well as the massive increase of the pressure with the second switch can be observed.

The determined effects are confirmed by the spectroscopic measurements as well. Figure 19 exemplarily shows two spectra at a distance of 40.7 mm from the inner tube of the IPG3. During the second switch, the intensity of the oxygen triplet at 777 nm increases by the factor of 10. Other intensities, such as the line at 615 nm, increase even by 100. The molecular intensities are too low to enable a more detailed investigation based on these data. The discrete increase during the transition implies that there are effects caused by dissociation or ionization processes, or temperature increase, or by an unknown combination of these. However the authors favor that the process is dominated by an increase of electrons as outlined earlier.

In Fig. 20, a major effect can be seen. The stepwise increase of the power results in a movement of the maximum along the tube radius. Here, the thick curves represent the intensities in the second operational regime whereas the thinner and dashed lines indicate the third regime. For the second switch, a jumpy movement

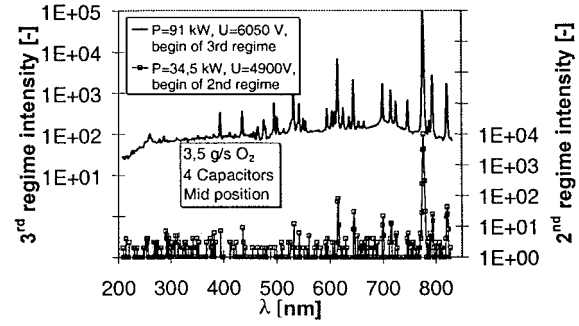

Fig. 19 Oxygen spectra at $r = 40.7$ mm (almost middle) using four capacitors ($f = 0.73$ MHz) for 3.5 g/s O_2.

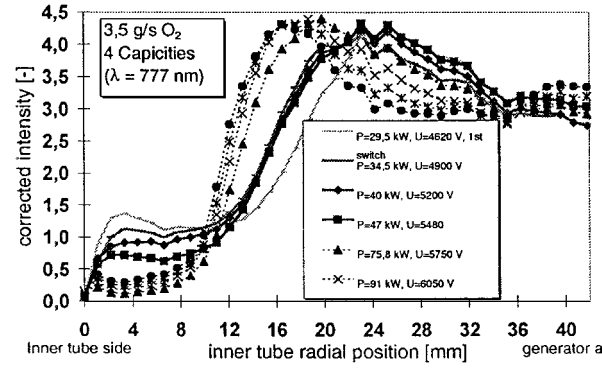

Fig. 20 Normalized radial intensity distribution for the oxygen triplet at 777 nm using four capacitors ($f = 0.73$ MHz) for 3.5 g/s O_2, depending on P_A.

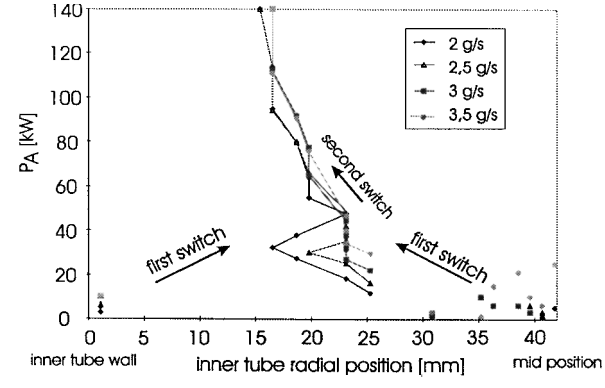

Fig. 21 Position of intensity maxima for the oxygen triplet at 777 nm with four capacitors ($f = 0.73$ MHz) for different mass flows vs P_A.

of the maximum toward the inner tube wall can be seen. This effect can be most likely explained by a change of the skin depth with increasing electrical conductivity [Eq. (11)]. It is evident that the share of intensity at the tube wall decreases with the second switch. However, the maximum of intensity moves farther left. Therefore, the left side slope of the curves after the switch increases. The first switch is not documented in detail in this paper. Nevertheless, these investigations and previous investigations with air[10] showed that the mode before the first switch has its maximum in the middle of the tube and at the inner tube wall. The middle maximum almost disappears with the first switch (also see Fig. 21).

The power histories, for example, the calorimetric power in the chamber, the behavior of P_{tube}, the shift from the tube wall shown in Fig. 20, and the intensity increase shown in Fig. 21 appear simultaneously. These observed high-power increases (depending on mass flow rates) show that there is an increase of electrical conductivity of the plasma that can also be seen by the overall move of the intensity maximum toward the inner tube wall. When Eq. (22) is considered, it can be concluded that the radial Lorentz forces must increase as

well by about the same factor. Perhaps this leads to an electromagnetically induced effect or even flow that leads to the decrease of the tube's heat load. Such effects have been calculated, for example, by Boulos et al.[18] In their work, electromagnetically induced flows that supported vortex flows in the tube of an rf plasma source were simulated and discussed.

In Figs. 22 and 23, the anode power and P_{tube} using one capacitor ($f = 1.46$ MHz) are shown. In comparison with Fig. 15 the corresponding cooling powers seem to be higher. This may be explained by a better power input due to the higher frequency. Additionally, the decrease of skin depth could probably be responsible for the increase. No second switch was observed for 2 g/s, whereas the second switch for 3 g/s came slightly later and more gradually than in the case of the 730-kHz operation. When it is assumed that the effect is due to the Lorentz force, this may be explained using the Eq. (22), which indicates that the Lorentz forces can decrease with higher frequencies. Here, further investigations such as the measurement of additional mass flow conditions, spectroscopy, and, in particular, calorimetric measurements (the Lorentz forces depend on P_{ind} as well) could lead to a better understanding.

In Fig. 24, a sintered silicon carbide (SSiC) material sample is shown in an oxygen plasma. Here, the sample reached wall temperatures of about 1200°C. Such experiments were performed within the Future European Space Transportation Program (FESTIP) to investigate the catalytic behavior at a constant condition by the combination of SSiC material tests with heat flux measurements.

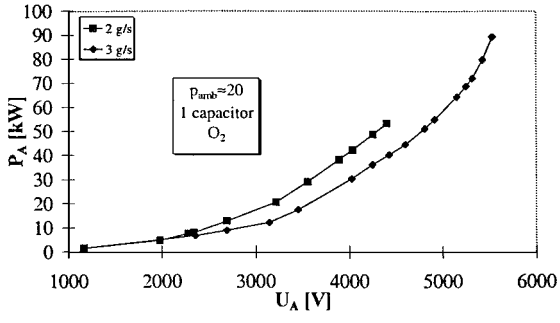

Fig. 22 P_A vs U_A for O_2 plasmas using one capacitor ($f = 1.45$ MHz) for different gas mass flows.

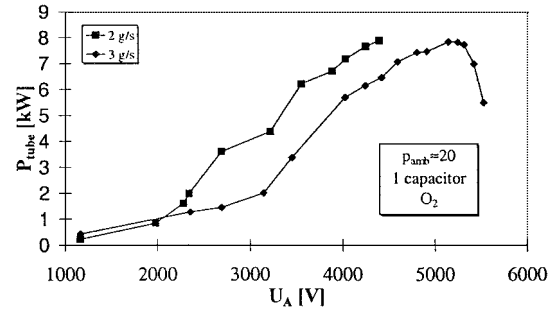

Fig. 23 P_{tube} vs U_A for O_2 plasmas using one capacitor ($f = 1.45$ MHz) for two different gas mass flows.

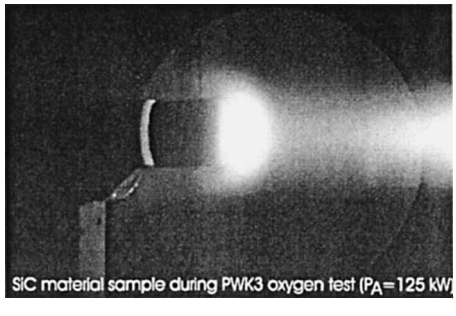

Fig. 24 PWK3–IPG3 oxygen plasma material test for the investigation of catalytic behavior: $T_{wall} \approx 1200°$C, four capacitors, and $L \approx 2$ mH.

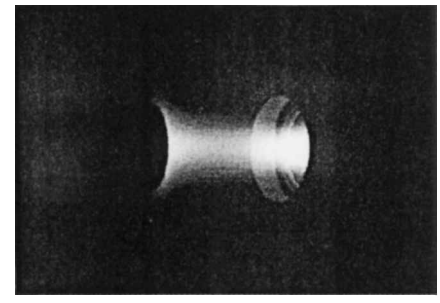

Fig. 25 PWK3–IPG3 operation; oxygen mass flow: 2.5 g/s, P_A = 91.5 kW, $p_\infty \approx 20$ Pa, and $x = 140$ mm.

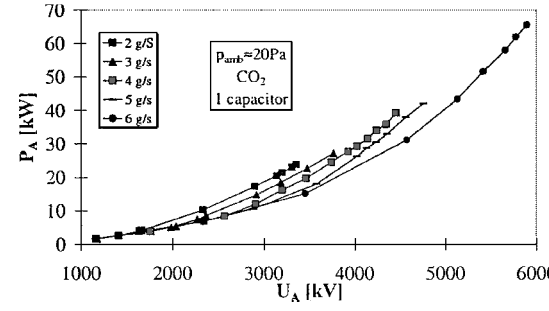

Fig. 26 P_A vs U_A for CO_2 plasmas using one capacitor ($f = 1.45$ MHz) for different mass flow rates.

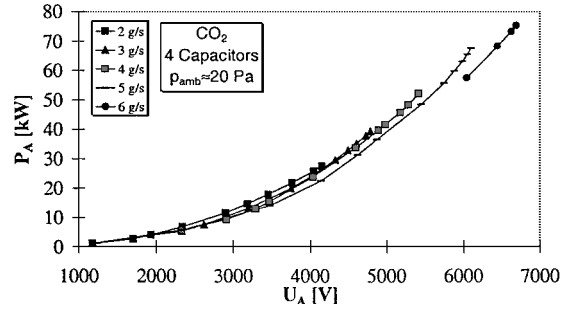

Fig. 27 P_A vs U_A for CO_2 plasmas using four capacitors (f = 0.73 MHz).

Figure 25 shows PWK3-IPG3 in operation using pure oxygen atmosphere. All operations were in the second mode. The second of the images implies the second mode operation, as the beam seems to have a minimum cross area at the outlet of the plasma generator. Additionally, the cross section appears to be lower than the tube cross section.

Experimental Results with CO_2

Apart from the second switch, the overall behavior with CO_2 is quite comparable with the O_2 behavior (Figs. 26 and 27). However, the plasma power related data, such as the heat fluxes, are lower for the same facility conditions. Furthermore, the tube cooling seems to be higher. The presented measurements show that heat fluxes in the range of several megawatts per square meter are possible. Measurements with tube cooling up to 11 kW and heat fluxes up to 2 MW/m^2 have been performed successfully. Corresponding measurements are included in a followup paper.[19] The histories of the tube cooling show the typical behavior of the first switch. (See Fig. 28 for four capacitors and Fig. 29 for one capacitor.) The curves are more or less identical as long as the power is below the transition power of the first switch. This can also be seen for the anode powers. One explanation for this behavior may be that the plasma has a very low electrical conductivity below the first switch. Therefore, it does not yet represent a real load for the electromagnetic field. The radial intensities (see also Ref. 10 for air) have maxima in the middle of the plasma tube as long as the first switch is not reached.

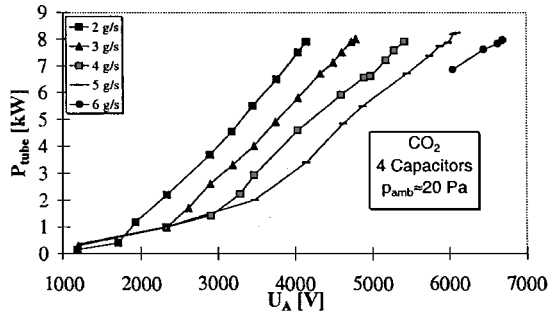

Fig. 28 P_{tube} vs U_A for CO_2 plasmas using four capacitors (f = 0.73 MHz).

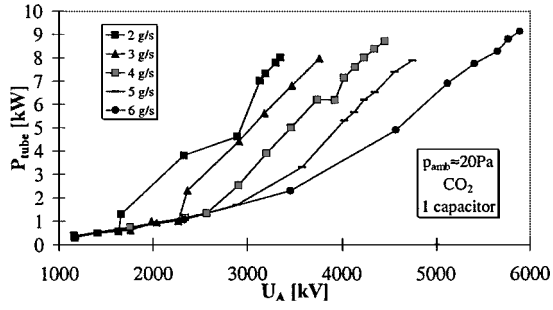

Fig. 29 P_{tube} vs U_A for CO_2 plasmas using one capacitor (f = 1.45 MHz) for different mass flow rates.

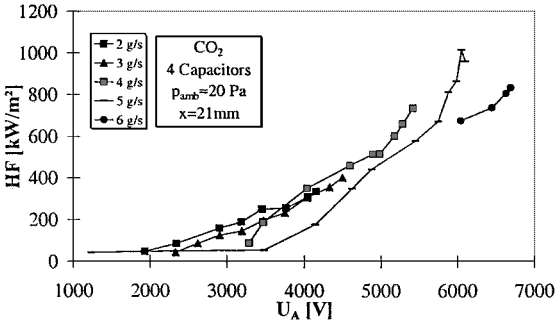

Fig. 30 Heat flux vs U_A for CO_2 plasmas using four capacitors (f = 0.73 MHz) for different mass flow rates.

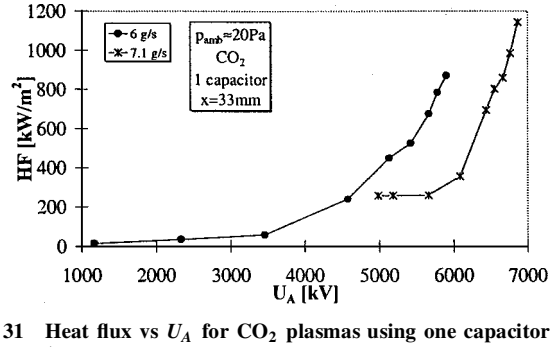

Fig. 31 Heat flux vs U_A for CO_2 plasmas using one capacitor (f = 1.45 MHz) for two different mass flow rates.

The power and all related measured values seem to be higher in the case of high frequency ($f = 1.45$ MHz) at the same U_A. When the plasma is assumed as secondary coil, the result is that the induced current amplitude is about proportional to the frequency. This is most likely an explanation for the higher powers within the higher frequency operation. However, the decreasing skin depth may counteract this effect because high power modes may be accompanied by increased tube cooling. (Compare Figs. 28 and 29.) This seems to be no severe problem as IPG3 has been qualified for tube cooling up to 11 kW and heat flux levels in the range of 1.2 MW/m^2 in CO_2 operation (Figs. 30 and 31). Further investigations were made, which have been presented in Ref. 19.

Summary

The first high-enthalpy tests with IPG3, developed for basic TPS material investigations using O_2 and CO_2 as working gases, were conducted. IPG3's design enables extensive investigations of the operational behavior of the plasma generator, of the characteristics of the plasma generated in the plasma tube and the chamber, and of materials to be used for atmospheric entries of spacecraft.

The operational behavior of IPG3 was measured in terms of the discharge behavior in combination with the ongoing histories of properties such as P_A, thermal powers, heat fluxes, and intensities. Two discrete switches were observed, which represent the jumpy transition from the first to the second and from the second to the third discharge mode. The discrete power increases (P_A and P_{cal}) in the second transition, the ongoing decrease of P_{tube}, the simultaneous sudden increase of the inner tube pressure (dissociation and/or ionization and/or temperature increase), and the observed movement of the radial intensity profile imply that the second transition is accompanied by a jumpy increase of the plasma's electrical conductivity. The decreasing tube cooling power suggests that there is a stabilization effect, perhaps driven by the increased Lorentz force, as explained in the analytical model. Later investigations, not presented in this paper, using different injection rings showed that this effect also depends on the swirl gas flow.[19]

Future interplanetary missions[4–7] as well as future plans to reach Mars with crewed spacecraft make it necessary to establish ground-based entry simulation facilities that enable the simulation of CO_2 (Mars, Venus) as well as CH_4 dominated atmospheric entries (Titan, see also Ref. 19). It has been shown that the PWK3–IPG3 facility is able to simulate such atmospheric entries, at least in terms of heat fluxes and the low-pressure regime of related trajectories. (See the inner tube pressures, which provide upper limits for the total pressures in the plasma beam.) Furthermore, basic material and plasma investigations using pure oxygen plasmas are being performed successfully within FESTIP.

Further investigations for different gases, in combination with planned coil current measurements, will be performed to simplify the comparison with numerical results.

Acknowledgments

The authors thank all members of the IRS plasma wind tunnel group. Thanks are extended to the Future European Space Transportation Program, which initiated a part of the work performed in this paper.

References

[1] Auweter-Kurtz, M., Kurtz, H. L., and Laure, S., "Plasma Generators for Reentry Simulation," *Journal of Propulsion and Power*, Vol. 12, No. 6, 1996, pp. 1053–1061.

[2] Stöckle, T., Auweter-Kurtz, M., and Laure, S., "Material Catalysis in High Enthalpy Air Flows," AIAA Paper 96-1904, 1996.

[3] Herdrich, G., Auweter-Kurtz, M., Hartling, M., and Laux, T., "PYREX-KAT38: Temperature Measurement System for the X-38 Nose Structure TPS," *2nd International Symposium on Atmospheric Reentry Vehicles and Systems*, Association Aeronautique et Astronautique de France, Les Mureaux, France, March 2001.

[4] Maraffa, L., Smith, A., Santovincenzo, A., Rouméas, R., Huot, J.-P., and Scoon, G., "Aerothermodynamics Aspects of Venus Sample Return Mission," 3rd European Symposium on Aerothermodynamics for Space Vehicles, ESA SP-426, European Space Research and Technology Center, Noordwijk, The Netherlands, Nov. 1998.

[5] Rubio Garcia, V., Maraffa, L., Scoon, G., Rouméas, R., and Seiler, R., "Mars Mini-Probes. Elements of Aerothermodynamics and Entry Trajectories," 3rd European Symposium on Aerothermodynamics for Space Vehicles, ESA SP-426, European Space and Technology Center, Noordwijk, The Netherlands, Nov. 1998.

[6] O'Neil, W., and Cazeau, C., "The Mars Sample Return Mission," International Astronautical Federation, IAF Rept. 99-Q.3.02, Oct. 1999.

[7] Pauly, K., Knuth, S., Hettmer, M., and Kalkum, F., "Die Mars Society Mars Ballon Mission," Deutscher Luft- und Raumfahrtkongreß 2001 (Conf.),

Deutsche Gesellschaft für Luft- und Raumfahrttechnik, Paper DGLR-JT2001-131, Hamburg, Germany, Sept. 2001.

[8]Auweter-Kurtz, M., Feigl, M., and Winter, M., "Diagnostic Tools for Plasma Wind Tunnels and Re-entry Vehicles at the IRS," Measurement Techniques for High Enthalpy and Plasma Flows Course, NATO Research and Technology Organization, Neuilly-sur-Seine, France, RTO EN-8, 1999, pp. 2B1–2B78.

[9]Wantuck, P., and Watanabe, H., "Radio Frequency (RF) Heated Supersonic Flow Laboratory," AIAA Paper 90-2469, July 1990.

[10]Herdrich, G., Auweter-Kurtz, M., and Kurtz, H. L., "New Inductively Heated Plasma Source for Reentry Simulations," *Journal of Thermophysics and Heat Transfer*, Vol. 14, No. 2, 2000, pp. 244–249; also AIAA Paper 98-3022, June 1998.

[11]Vilbig, F., *Lehrbuch der Hochfrequenztechnik*, Vol. 2, Akademische Verlagsges, Frankfurt, 1958, pp. 77–87.

[12]"Technical Specification of the RF-Capacitors and the Triode RS 3300 CJ of the PWK3-IPG Energy Supply," Fritz Düsseldorf Gesellschaft mit beschrānkter Haftung, 1997.

[13]Mostaghimi, J., and Boulos, M. I., "Two-Dimensional Electromagnetic Field Effects in Induction Plasma Modelling," *Plasma Chemistry and Plasma Processing*, Vol. 9, No. 1, 1989, pp. 25–44.

[14]Stöckle, T., Auweter-Kurtz, M., and Laure, S., "Material Catalysis in High Enthalpy Air Flows," AIAA Paper 96-1904, June 1996.

[15]Winter, M., and Auweter-Kurtz, M., "Emission Spectroscopic Investigation of the Boundary Layer in Front of a Blunt Body in a Subsonic Air Plasma Flow," 3rd European Symposium on Aerothermodynamics for Space Vehicles, ESA SP-426, European Science and Technology Center, Noordwijk, The Netherlands, Nov. 1998.

[16]Mekideche, M. R., "Contribution à la modélisation numérique de torches de plasma d'induction," Ph.D. Dissertation, Lab. de Recherche Techniques Inductives, École Doctorale Sciences pour L'ingénieur de Nantes, Nantes, France, Oct. 1993.

[17]Fasholz, J., Decker, E., and Röttgen, H., *Induktive Erwärmung*, 4th ed., RWE Aktiengesellschaft, Essen, Germany, 1991.

[18]Boulos, M. I., Gagne, R., and Barnes, R., "Effect of Swirl and Confinement on the Flow and Temperature Fields in an Inductively Coupled r.f. Plasma," *Canadian Journal of Chemical Engineering*, Vol. 58, June 1980, pp. 367–375.

[19]Herdrich, G., Auweter-Kurtz, M., Kurtz, H., Laux, T., and Schreiber, E., "Investigation of the Inductively Heated Plasmagenerator IPG3 Using Injection Rings of Different Geometries," AIAA Paper 2000-2445, June 2000.